THE ASTROPHYSICAL JOURNAL, 547:172–186, 2001 January 20
© 2001. The American Astronomical Society. All rights reserved. Printed in U.S.A.

NUMERICAL MODELS OF THE MULTIPHASE INTERSTELLAR MATTER WITH STELLAR ENERGY FEEDBACK ON A GALACTIC SCALE

KEIICHI WADA[1] AND COLIN A. NORMAN[2]
Johns Hopkins University, Baltimore, MD 21218
Received 2000 May 4; accepted 2000 August 25

ABSTRACT

High-resolution two-dimensional hydrodynamic simulations for the interstellar matter (ISM) in a galactic disk are enhanced to include explicitly star formation and the feedback effects from supernovae and stellar winds. A globally stable multiphase ISM is formed, in which filamentary and clumpy structure is a characteristic feature. We find a new component of 10^6–10^8 K gas that is a direct consequence of the energy input from the feedback. The total supernovae rate in the system varies by an order of magnitude over a timescale of 10^6 yr. The evolution of the supernovae rate exhibits chaotic behavior because the star formation is triggered by supernovae explosions in the inhomogeneous interstellar medium. We also find that, in spite of its very complicated spatial structure, the multiphase ISM exhibits a one-point probability density function (pdf) that is a perfect lognormal distribution over four decades in density, 10^2–10^6 $M_\odot$ pc^{-2}. The lognormal pdf is very robust even in regions with frequent bursts of supernovae. Low-density regions or cavities (<10 $M_\odot$ pc^{-2}), on the other hand, exhibit the normal Gaussian distribution. These characteristic pdf's are achieved over a local dynamical scale. The energy spectra are $E(k) \propto k^{-3}$ without feedback and $E(k) \propto k^{-2}$ including stellar energy feedback.

Subject headings: galaxies: structure — ISM: kinematics and dynamics — ISM: structure — methods: numerical

1. INTRODUCTION

Construction of relevant numerical models of the multiphase interstellar matter (ISM) with realistic cooling and heating processes is crucial for serious numerical simulations of galaxies that include star formation. Such simulations will significantly enhance our understanding of galaxy formation and evolution. However, the current numerical models for star formation on a galaxy scale are still based on many ad hoc assumptions and are essentially phenomenological models. For example, the ISM is often represented by an isothermal gas at temperature $T = 10^4$ K or equivalently a sound velocity ~ 10 km s^{-1} in Euler-mesh simulations. Alternatively, the ISM can be assumed to be a complex of inelastic particles. Incorporating the effects of star formation into such simple models of the ISM still requires that one cannot avoid many phenomenological assumptions (cf. Shore & Ferrini 1995). For instance, accurately representing supernovae (SNe) is crucial for modeling stellar energy feedback to the ISM. Evolution of supernova remnants in turbulent and inhomogeneous media must be very different from the simple symmetric evolution often assumed and cannot be represented by a simple analytic solution, such as the Sedov solution.

Numerical studies of the multiphase ISM based on hydrodynamic simulations have been tried by several groups (e.g., Bania & Lyon 1980; Rosen, Bregman, & Norman 1993; Rosen & Bregman 1995; Vázquez-Semadeni, Pasot, & Pouquet 1995; Gerritsen & Icke 1997). Dynamics of the multiphase ISM have been studied by Rosen et al. (1993) and Rosen & Bregman (1995). Their simulations are for two fluids (gas and stars) in two dimensions ignoring self-gravity of the gas and the effects of galactic rotation. Self-gravity of the gas is necessary to produce very high density clouds which are the sites of star formation. Rotation around the galactic center is an important element for the global gasdynamics and ISM structure. Vázquez-Semadeni et al. (1995) and Passot, Vázquez-Semaden, & Pouquet (1995) have studied self-gravitating supersonic turbulence with two-dimensional hydrodynamic and magnetohydrodynamic simulations. They also took into account Coriolis force and large-scale shear. However, periodic boundaries with a local-shearing coordinate were assumed. An artificial mass diffusion term in the continuity equation was assumed, and, as discussed in their paper, this term smooths out the density gradients and prevents the generation of large density contrasts and strong shocks. All of these previous simulations are "local" models.

Wada & Norman (1999, hereafter Paper I) presented a high-resolution numerical model of the multiphase ISM in a central 2 kpc region of a disk galaxy. We used an Eulerian hydrocode without periodic boundary conditions. We assume a thin disk, and use 1024^2 meshes for a 4 kpc^2 region around the galactic center. We take into account self-gravity of the gas and radiative cooling and heating due to UV background radiation. The main result of Paper I is that a globally stable, multiphase ISM is formed as a natural consequence of the nonlinear evolution of thermal and gravitational instabilities in the gas disk. The density ranges over 7 orders of magnitude from 10^{-1} to 10^6 $M_\odot$ pc^{-2}, and the temperature extends over five decades from 10 to 10^6 K. We found in Paper I that the ISM cannot be expressed simply by the two-phase or three-phase model (e.g., McKee & Ostriker 1977; Ikeuchi, Habe, & Tanaka 1984; Norman & Ikeuchi 1989; Norman & Ferrara 1996) because gasdynamic processes such as turbulence, global rotation, shear motion, and shocks are important as well as thermal processes. Our high-resolution Eulerian hydrodynamic code allows us to handle gasdynamics on a kiloparsec scale with a resolution of a few parsecs regardless of the gas density. Possible star-forming sites where the gas

[1] Present address: National Astronomical Observatory, Mitaka 181-8588, Japan; wada.keiichi@nao.ac.jp.
[2] Space Telescope Science Institute, Baltimore, MD 21218.

density is very high ($n \gtrsim 10^4$ cm^{-3}) and the temperature is less than 100 K can be directly identified from the results. The multiphase gaseous structure is very complicated and is characterized by filamentary and clumpy substructure as well as by low-density holes and voids surrounded by the denser media.

In this paper, we modify the numerical code in Paper I to explicitly include star formation and the feedback effects from supernovae and stellar winds from massive stars. We succeed in constructing globally stable multiphase ISM disks, in which birth and death of massive stars are consistently implemented.

This paper is organized as follows. In § 2 we give a detailed description of our numerical code and models. In § 3 various test results are presented. The global structure and evolution of the self-gravitating multiphase disk with and without stellar energy feedback are discussed in § 4. The statistical nature of the media in a quasi-stable state, namely, the probability density functions and the energy spectra, is discussed in § 5. Implications of the results are discussed in § 6. Finally conclusions are presented in § 7.

2. NUMERICAL METHODS AND MODELS

In order to model the global evolution of the multiphase ISM, a hydrodynamic code must deal with a wide dynamic range (e.g., scale: 1 pc–few kpc; density: 10^{-3} to 10^6 cm^{-3}; and temperature: 10–10^8 K). Moreover, shocks must be resolved correctly, because typical Mach numbers range from 10 to 100 in the ISM of a galaxy, and also SNe and stellar winds cause strong shocks with Mach numbers of several 100. Smooth particle hydrodynamics (SPH) is at present one of the most widely used hydrodynamic codes for simulations of galaxy formation. However, SPH is not suitable for the highly developed, multiphase ISM with strongly shocked gas because of its relatively poor resolution for the diffuse gas. To understand the structure of the multiphase ISM, we need high spatial resolution for the hot, diffuse gas as well as for the cold, dense gas.

We use hydrodynamic simulations for a single fluid taking into account the self-gravity of the gas and radiative cooling and heating processes. The multiphase feature of the gas, that is, the multitemperature and multidensity structure, should be achieved as a result of the nonlinear evolution of a single fluid, if we take into account realistic cooling and heating processes, and the self-gravity of the gas with relevant spatial resolution. In order to investigate the effects of the global dynamics of the gas, the evolution of the whole rotating disk is simulated. The hydrodynamic part of the simulations is solved by a high-accuracy explicit Eulerian code with nonadaptive grids. The effect of the radiative cooling is implemented using an implicit method with a cooling function. The numerical code is tested for various standard problems (see details in § 3).

2.1. *Basic Equations and Numerical Scheme*

We solve the following equations numerically in two dimensions:

$$\frac{\partial \rho}{\partial t} + \nabla \cdot (\rho \boldsymbol{v}) = 0 , \tag{1}$$

$$\frac{\partial \boldsymbol{v}}{\partial t} + (\boldsymbol{v} \cdot \nabla)\boldsymbol{v} + \frac{\nabla p}{\rho} + \nabla \Phi_{\rm ext} + \nabla \Phi_{\rm sg} = 0 , \tag{2}$$

$$\frac{\partial E}{\partial t} + \frac{1}{\rho} \nabla \cdot [(\rho E + p)\boldsymbol{v}] = \Gamma_* + \Gamma_{\rm UV} - \rho \Lambda(T_g) , \tag{3}$$

$$\nabla^2 \Phi_{\rm sg} = 4\pi G \rho , \tag{4}$$

where ρ, p, and $\boldsymbol{v}$ are density, pressure, and velocity of the gas, and the specific total energy $E \equiv |\boldsymbol{v}|^2/2 + p/(\gamma - 1)\rho$. The ratio of specific heat at constant pressure and volume, γ, is an arbitrary constant. Especially under a limited spatial resolution ($\sim$2 pc), the effective γ would not be either $\gamma = 5/3$ or $\gamma = 1$. The γ should be determined by the local physical conditions in the ISM, assuming a constant γ for the multiphase medium would not be realistic. However, here we assume for simplicity $\gamma = 1.4$. We confirmed that our results are not sensitive to the value of γ because the turbulent pressure dominates the thermal pressure.

We assume a time-independent external potential

$$\Phi_{\rm ext} \equiv \frac{-GM_g}{(R^2 + a^2)^{1/2}} = -\left(\frac{27}{4}\right)^{1/2} \frac{v_c^2}{(R^2 + a^2)^{1/2}} ,$$

where $a = 200$ pc is a core radius of the potential and $v_c = 150$ km s^{-1} is the maximum rotational velocity. These parameters are chosen to resemble the rotation curve of typical spiral galaxies (Sofue et al. 1999). We also assume a cooling function $\Lambda(T_g)$ (10 K $< T_g < 10^8$ K) and a heating function Γ_* (see also § 2.2).

The hydrodynamic part of the equation is solved by second-order advection upstream splitting method (AUSM) based on Liou & Steffen (1993). We summarize the essential points of AUSM below.

The hydrodynamic part of the basic equations are written as

$$\frac{\partial \boldsymbol{U}}{\partial t} + \frac{\partial \boldsymbol{F}}{\partial x} + \frac{\partial \boldsymbol{G}}{\partial y} = 0 , \tag{5}$$

where

$$\boldsymbol{U}^T \equiv (\rho, \rho u, \rho v, \rho E) ,$$

$$\boldsymbol{F}^T \equiv [\rho u, \rho u^2 + p, \rho uv, u(\rho E + p)] ,$$

$$\boldsymbol{G}^T \equiv [\rho v, \rho vu, \rho v^2 + p, v(\rho E + p)] .$$

Flux $\boldsymbol{F}$ and $\boldsymbol{G}$ consist of two physically distinct parts, namely, advection and pressure terms:

$$\boldsymbol{F} = \begin{pmatrix} \rho \\ \rho u \\ \rho v \\ \rho H \end{pmatrix} u + \begin{pmatrix} 0 \\ p \\ 0 \\ 0 \end{pmatrix}, \quad \boldsymbol{G} = \begin{pmatrix} \rho \\ \rho u \\ \rho v \\ \rho H \end{pmatrix} v + \begin{pmatrix} 0 \\ 0 \\ p \\ 0 \end{pmatrix} , \tag{6}$$

where the enthalpy $H \equiv E + p/\rho$.

Paying attention to this, in AUSM, these two terms are separately split at a cell surface. As a result, the scheme is remarkably simple, but it is accurate enough compared to the flux-difference splitting scheme such as Roe splitting (Roe 1981).

The van Leer–type flux splitting process is applied separately to these two terms. According to Liou (1996), the split of Mach number, M, and pressure that we adopt here are

$$\mathcal{M}^{\pm}(M) = \begin{cases} \frac{1}{2}(M \pm |M|) & \text{if } |M| \geq 1 , \\ \pm \frac{1}{4}(M \pm 1)^2 \pm \frac{1}{8}(M^2 - 1)^2 & \text{otherwise ;} \end{cases} \tag{7}$$

$$p^{\pm}(M) = \begin{cases} \dfrac{p}{2}\,[1 \pm \mathrm{sign}(M)] & \text{if } |M| \geq 1\,, \\ \pm\dfrac{p}{4}\,(M \pm 1)^2(2 \mp M) \pm \dfrac{3p}{16}\,M(M^2-1)^2 & \text{otherwise}\,. \end{cases} \tag{8}$$

AUSM works very well for adiabatic flow with low Mach number. However, this is not the case for the highly supersonic flows with strong cooling, such as the ISM in galaxies that we are studying in this paper. Since the kinetic energy of the gas sometimes dominates the thermal energy in such flows, it is often difficult to avoid negative pressure at a grid point due to numerical errors. Therefore, if the pressure at a cell derived from the total energy E becomes negative in the postshock region, we calculate pressure p from

$$\frac{\partial S}{\partial t} + \nabla \cdot (S\boldsymbol{v}) = 0\,, \tag{9}$$

where "modified entropy," S, is defined as $S \equiv p/\rho^{\gamma-1}$ (Ryu et al. 1993), instead of the energy equation

$$\rho\,\frac{\partial E}{\partial t} + \nabla \cdot [(\rho E + p)\boldsymbol{v}] = 0\,. \tag{10}$$

To identify the postshock regions, we use the same criteria as those in Ryu et al. (1993).

The entropy flux $\rho S\boldsymbol{v}$ is split in the same way as for the total energy flux $(\rho E + p)\boldsymbol{v}$ at cell interfaces. We found that this modification works very well and is stable for the ISM with frequent supernova explosions.

We achieve third-order spatial accuracy with the monotone upstream-centered schemes for conservation laws (MUSCL) approach (van Leer 1977). To satisfy the total variation diminishing (TVD) condition using MUSCL, we introduce a limiting function:

$$(Q_L)_{j+1/2} = Q_j + \tfrac{1}{4}[(1-\kappa)\tilde{\Delta}_- + (1+\kappa)\tilde{\Delta}_+]_j\,, \tag{11}$$

$$\tilde{\Delta}_+ \equiv \mathrm{minmod}(\Delta_+, b\Delta_-)\,, \tag{12}$$

$$\tilde{\Delta}_- \equiv \mathrm{minmod}(\Delta_-, b\Delta_+)\,, \tag{13}$$

where $b = (3-\kappa)/(1-\kappa)$. The parameter κ can be $\kappa = -1$, 0, or $\frac{1}{3}$, which represent second-order fully upwind, second-order upwind biased, and third-order upwind biased cases, respectively. After the test calculations, we decided to use $\kappa = \frac{1}{3}$. The right state, $(Q_R)_{j+1/2}$, is evaluated similarly by using the data of points $j, j+1$, and $j+2$.

After testing this code for various hydrodynamic problems (see § 3), we find that AUSM with MUSCL is a potentially powerful scheme for astrophysical problems as the piecewise parabolic method (PPM) (Woodward & Colella 1984), but the algorithms and coding are much simpler than PPM.

We use 1024^2 Cartesian grid points for calculating gasdynamics in a 2×2 kpc region which includes the galactic center. Therefore the spatial resolution is 1.95 pc.

The gravitational potential of the gas $\Phi_{i,j}$ at a mesh point (i, j) can be written as

$$\Phi_{i,j} = \sum_{i',j'} \mathscr{G}_{i-i',j-j'}\,\sigma_{i',j'}\,, \tag{14}$$

where $\mathscr{G}$ is the Green's function of point-mass gravity and $\sigma_{i',j'}$ is the surface density at a mesh point (i, j).

In order to calculate $\Phi_{i,j}$ in equation (14), we use the convolution method with the fast Fourier transform (Hockney & Eastwood 1981). In this method, 2048^2 grid cells and a periodic Green's function $\mathscr{G}$ are used to calculate the self-gravity of the isolated matter in the 1024^2 grid points.

Time integration for advective terms of equations (1), (2), and (3) is achieved by the second-order leap-frog method. Each time step δt is determined by the Courant condition:

$$\delta t = C/\sqrt{\max\,(t_1^{-2}, t_2^{-2}, t_3^{-2}, t_4^{-2})}\,, \tag{15}$$

where C is a constant ~ 0.5, and

$$t_1 \equiv \Delta/c_s\,, \quad t_2 \equiv \Delta/\max\,(|\boldsymbol{u}|)\,, \quad t_3 \equiv \Delta/\max\,(|\boldsymbol{v}|)\,, \tag{16}$$

$$t_4 \equiv \sqrt{|\boldsymbol{v}|/\sqrt{|\nabla\Phi_{\mathrm{sg}}|^2 + |\nabla\Phi_{\mathrm{ext}}|^2}}\,, \tag{17}$$

where Δ is size of a single grid cell and c_s is sound velocity. The explicit time integration, however, is not suitable for the source terms, especially the radiative cooling, because the cooling time becomes very short in high-density regions. Therefore we adopt implicit time integration for the cooling term, that is, we find a solution for the following equation iteratively:

$$(\rho E)_{i,j}^{n+1} - (\rho E)_{i,j}^{n} + \delta t(\rho_{i,j}^{n})^2\Lambda(T_{i,j}^{n}) = 0\,, \tag{18}$$

where n denotes time steps.

The initial conditions are an axisymmetric and rotationally supported disk, whose radius is 700 pc, with the Toomre stability parameter $Q \equiv \kappa c_s/\pi G\Sigma_{g,0} = 1.2$ over the whole disk, where κ, c_s, and $\Sigma_{g,0}$ are the epicyclic frequency for the external potential, the sound velocity of the gas corresponding to $T_g = 10^4$ K, and the initial surface density of the gas, respectively. The initial rotational velocity is chosen in order to balance the centrifugal force caused by the external potential Φ_{ext} and Φ_{sg}.

Random density fluctuations are added to the initial disk, with an amplitude less than 1% of the unperturbed density and temperature. The initial temperature is set to 10^4 K over the whole region. In ghost zones at boundaries, the physical values remain at their initial values during the calculations. From test runs, we found that these boundary conditions are much better than so-called outflow boundaries, because the latter cause strong unphysical reflection of waves at the boundaries.

2.2. *Cooling and Heating Processes*

We use the cooling curves of Spaans & Norman (1997) (Fig. 1). The cooling functions simplify the implementation of cooling by collecting the effects of various coolants. The cooling processes taken into account are (1) recombination of H, He, C, O, N, Si, and Fe; (2) collisional excitation of H I, C I–IV, and O I–IV; (3) hydrogen and helium bremsstrahlung; (4) vibrational and rotational excitation of H_2; and (5) atomic and molecular cooling due to fine-structure emission of C, C^+, and O and rotational line emission of CO and H_2. We report results with $\Lambda(T_g)$ for solar metallicity in this paper. We have tested models with the cooling curve for 0.01 $Z_\odot$ metallicity, and the qualitative results are similar to the model with $Z = Z_\odot$. We will discuss the effects of the metallicity in subsequent papers. The maximum and minimum cutoff temperatures of the gas are set to be 10 and 10^8 K.

As well as the heating due to massive stars (see § 2.3), we assume a uniform UV radiation field and photoelectric

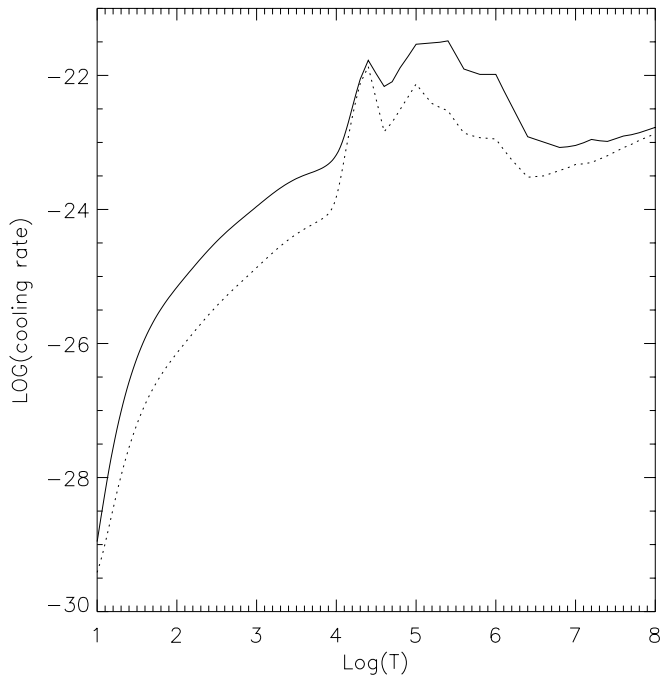

FIG. 1.—Cooling functions adopted for the calculation Λ/n_H^2 (ergs cm^3 s^{-1}). The solid line is for $Z = 1.0\ Z_\odot$, and the dashed line is for $Z = 0.1\ Z_\odot$.

heating of grains and polycyclic aromatic hydrocarbons (PAHs). The heating rate Γ_{UV} is the same as in Gerritsen & Icke (1997):

$$\Gamma_{UV} = 1.0 \times 10^{-24} \varepsilon G_0 \text{ ergs s}^{-1}\ , \qquad (19)$$

where the heating efficiency ε is assumed to be 0.05 and G_0 is the incident FUV field normalized to the local interstellar value.

2.3. *Star Formation and Energy Feedback*

We take into account two feedback effects of massive stars on the gasdynamics, namely, stellar winds and supernova explosions. We first identify cells which satisfy criteria for star formation. The criteria for each cell where star formation is allowed are the following: (1) The surface density is greater than the threshold for star formation $(\Sigma_g)_{i,j} > \Sigma_c$, (2) the temperature is less than the critical temperature $(T_g)_{i,j} < T_c$, and (3) criteria 1 and 2 must last for 10^5 yr. In these simulations we have chosen $T_c = 50$ K and $\Sigma_c = 5 \times 10^4\ M_\odot\ \text{pc}^{-2}$. Assuming the Salpeter initial mass function (IMF) with $m_u = 120\ M_\odot$ and $m_l = 0.2\ M_\odot$, we create test particles representing massive stars ($>8\ M_\odot$). Typically 10–100 massive stars are replaced by one test particle. The initial velocity of the test particles is taken to be the same as their parent gas. The kinematics of the test particles in the external potential and the self-gravitational potential of the gas are followed by the second-order time-integration method. The stars (test particles) inject energy due to stellar winds to the cells where the stars are located during their lifetime, which is approximately $\sim 10^7$ yr. The heating rate used is given by Leitherer, Robert, & Drissen (1992), in which solar metallicity is assumed. When the star explodes as a supernova, an energy of 10^{51} ergs is injected into the cell where the test particle is located. The cooling procedure is not used for such cells, but the cells adjoining the supernova cell are treated normally. Evolution of the supernova remnant depends on its environment.

In contrast to previous numerical studies of the ISM on a galaxy scale with supernovae explosions, we do not assume any evolutionary models for the supernova remnant (SNR) or for the heating efficiency of the ISM due to supernovae. The heating efficiency must differ in different environments. Nevertheless, it has been assumed as an ad hoc constant in previous simulations, and it varies in authors from 10^{-1} (Navarro & White 1993) to 10^{-4} (Hernquist & Mihos 1995). The other problem in implementing feedback from star formation in numerical codes is how to assign the feedback energy to the ISM. Two main methods have been used: enhancing the thermal energy of star-forming particles or cells (e.g., Katz 1992; Rosen & Bregman 1995; Mori et al. 1997), or giving some kinetic energy to the cells (e.g., Navarro & White 1993; Heller & Shlosman 1994). It is not clear, however, which method is better in simulations. Gerritsen & Icke (1997) has compared these two methods in their SPH simulations and found that assigning all energy to single gas particles gives better results. This problem is caused by lack of resolution. The resolution of most simulations is much larger than 10 pc. Since SNe explosions and stellar winds could affect the ISM over several tens or parsecs during about 10^7 yr, parsec-scale spatial resolution is necessary.

With our code, the two-dimensional evolution of blast waves caused by supernovae in an inhomogeneous and nonstationary medium with global rotation is followed explicitly. Therefore, we can follow consistently the thermal and dynamical evolution of the ISM in the environment of star-forming regions and the associated supernovae remnants and superbubbles (cf. Norman & Ikeuchi 1989).

3. TESTS OF THE NUMERICAL CODE

We have tested our code for a number of standard test calculations and compared the results to those with other high-accuracy codes in the literature or with analytical solutions. In the following sections, we briefly summarize the test calculations of one- and two-dimensional shocks, a point explosion in a uniform medium, resonantly driven spiral shocks in a weak bar potential, and linear and nonlinear evolution of spiral density modes in a self-gravitating disk. We found that our code is accurate enough to simulate the dynamics of a highly supersonic and self-gravitating gaseous flow with explosions.

3.1. *One-dimensional and Two-dimensional Tests for Shocks*

We have tested our code for two standard one-dimensional shock tests: the Sod shock-tube problem (Sod 1978) and two strong interacting shocks (Woodward & Colella 1984, hereafter WC84). We confirmed that the code captures shocks in a few zones and contact discontinuities in several zones without numerical postshock oscillations or overshoots. The numerical accuracy and the stability are as good as those by the TVD method (e.g., Harten 1983; Ryu et al. 1993), and by the PPM (WC84).

Even though our code shows very good results for the one-dimensional shock test, it does not necessarily mean that the code is suitable for two-dimensional problems. Here we show results for three test problems in two dimensions: (1) the double Mach reflection of a strong shock; (2) a point explosion in an adiabatic uniform medium; and (3) an isothermal gas flow in a weak barred potential.

The first test problem is the same problem described in WC84, which is the double Mach reflection of a Mach 10 shock from an inclined plane. Figure 2 shows the resulting density and temperature profiles at $t = 0.2$ with a resolution of $\Delta x = \Delta y = 1/120$. Although small noisy structures are observed behind the curved reflected shocks, for the strong shocks and other reflected shocks, we find good agreement between our result and the result with the PPM by WC84 and with ZEUS-2D by Stone & Norman (1992). We could remove the small noise behind the reflected shock, if we use van Leer's limiter, instead of the minmod limiter, equations (11)–(13). However, it makes the shocks and contact discontinuities unsharp.

The second two-dimensional test is for the evolution of a blast wave caused by a point explosion in an inhomogeneous and adiabatic medium. This test is important to judge the accuracy and feasibility for realistic models with supernovae explosion. The evolution of the shock front is analytically described by the two-dimensional Sedov-Taylor solution, $R_s(t) = (E/\Sigma)^{0.25} t^{0.5}$, where Σ is the surface density and E is energy of a point explosion. Figure 3 is time evolution of a radius of the blast wave. The numerical result coincides with the analytic solution correctly.

The above two tests are for shock propagation in a stationary medium. The final two-dimensional test is a rotating gas flow in a weak barlike potential. Gaseous response to the nonaxisymmetric potential has been well studied numerically (e.g., Athanassoula 1992; Wada & Habe 1992, 1995; Englmaier & Gerhard 1997) and analytically (e.g., Yuan & Cheng 1989; Wada 1994; Lindblad & Lindblad 1994). We therefore use this as a test problem. A rotating barlike potential causes resonances in orbits, and spiral-like shocks are formed. The model used here is the same as model B in Fukuda, Wada, & Habe (1998), in which an isothermal equation of state is assumed. In this model, a mass concentration in the galactic center such as a supermassive black hole causes a new Lindblad resonance (NLR) inside the ordinary *inner* ILR. This resonance has similar characteristics to the outer ILR, therefore two *trailing spirals* are generated near the NLR, as expected from analytic work (Wada 1994). Figure 4 shows the density distribution of the model at $t = 0.2$, which can be compared with Figure 5 in Fukuda et al. (1998). As expected, two trailing spiral shocks are formed, and the structure is quite similar

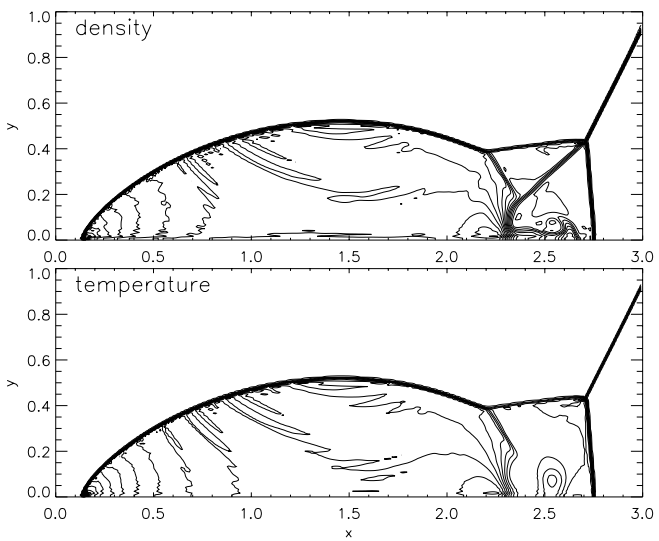

FIG. 2.—Two-dimensional test calculation (1): Double Mach reflection. Density (*top*) and temperature (*bottom*) at $t = 0.6$ are shown. The contour levels are the same as in Fig. 4 of Woodward & Colella (1984).

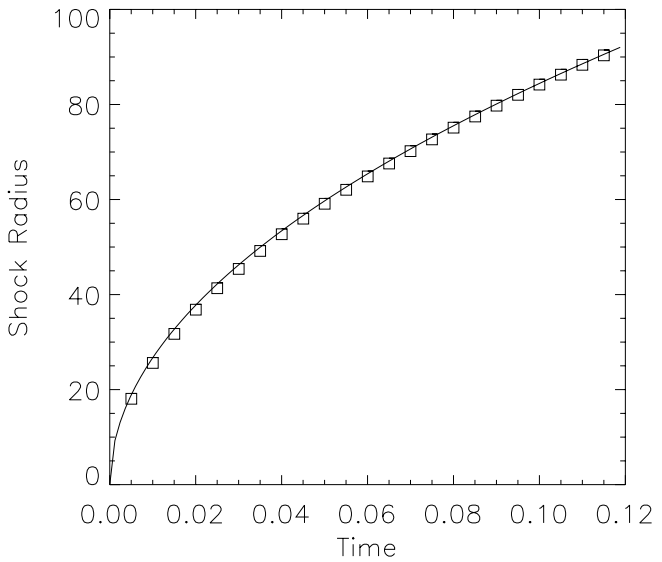

FIG. 3.—Two-dimensional test calculation (2): Evolution of a shock radius of a two-dimensional cylindrical explosion in an ideal gas with $\gamma = 5/3$ (*open squares*). The solid line is a two-dimensional Sedov-Taylor solution [$R_s(t) = (E/\Sigma_g)^{1/4} t^{1/2}$, where Σ_g is a surface density and E is energy of a point explosion].

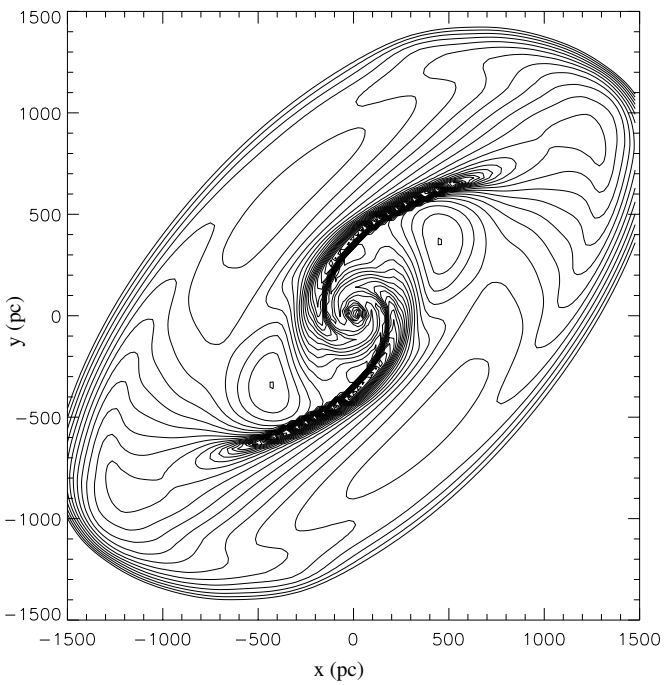

FIG. 4.—Two-dimensional test calculation (3): log-scaled gas density distribution at $t = 0.2$ in a weak bar potential, which is the same as model B in Fukuda et al. (1998), which is the SPH simulation. Thirty contours are drawn from log $\Sigma_g = 3$ to 4.5. The two spiral shocks are produced by a nuclear Lindblad resonance due to a bar potential. Our result is the same as the result with the SPH simulations by Fukuda et al. (1998).

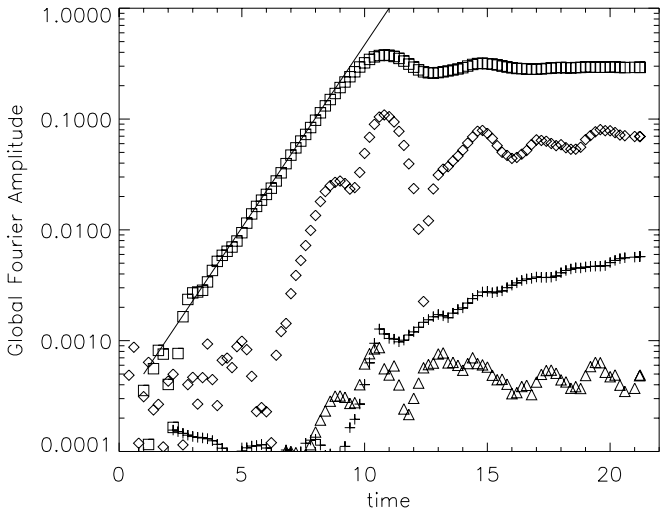

FIG. 5.—Evolution of the global Fourier amplitudes defined by eq. (20). Each mode is represented by the open boxes ($m = 2$), open diamonds ($m = 4$), plus signs ($m = 1$), and open triangles ($m = 3$). The growth rates and their saturation are almost the same as the results in Laughlin, Korchagin, & Adams (1997). The solid line is the growth rate expected from the linear analysis.

to the result with the SPH simulation by Fukuda et al. (1998).

3.2. *Evolution of Spiral Density Modes*

The tests so far are for a non–self-gravitating fluid. We confirmed that numerical solutions using the Poisson equation solver in our code are exactly the same as the analytic solutions for a point-mass distribution and for the Mestel disk. We show test results for a more practical problem: global stability of a self-gravitating disk. We examined gravitational instabilities in the same disk model as the reference model in Laughlin, Korchagin, & Adams (1998, hereafter LKA). The disk is a massive disk around a central star (the mass ratio is 1.5), and the initial surface density profile is $\Sigma_0(r) = 0.372 \exp [-(r - 0.45)^2/0.05]$. The inner and outer edges lie at $r = 0.25$ and 1.0. The polytropic equation of state is assumed, i.e., $p = 0.25\Sigma^{\gamma_p}$, where the polytropic constant $\gamma_p = 2$. We plot the development of the global Fourier amplitudes, C_m, for the modes with azimuthal wavenumbers $m = 1$, 2, 3, and 4 in Figure 5. The global Fourier amplitudes C_m are defined by

$$C_m = \frac{\left| \int_0^{2\pi} \int_{0.25}^{1.0} \Sigma(r, \phi) e^{-im\phi} r dr\, d\phi \right|}{\int_0^{2\pi} \int_{0.25}^{1.0} \Sigma(r, \phi) r dr\, d\phi} . \quad (20)$$

LKA used polar coordinates (256 × 256 zones), and reflecting boundary conditions were applied at both the inner and outer edge of the disk. In contrast, we used Cartesian coordinates (512 × 512 zones), and we did not solve the regions inside and outside the inner and outer boundaries. Therefore, the spatial resolution and boundary conditions are not strictly identical between these two simulations. The results, however, are surprisingly similar. The $m = 2$ unstable mode is the first growing mode, and the $m = 4$ mode grows with approximately twice the growth rate of the $m = 2$ mode. These growth rates and their saturation are almost the same in LKA. Moreover, the growth rate for the $m = 4$ mode expected from the linear analysis by LKA coincides with the numerical result very well.

4. RESULTS

4.1. *Evolution and Structure of a Highly Unstable Disk without Energy Feedback*

Figure 6 shows an initial 10 Myr evolution of a model without stellar energy feedback (model NSF). The rotational period at $R = 200$ pc is about 8 Myr. Density and temperature distributions in the central 1 × 1 kpc region are shown. Although the initial Toomre Q value is 1.2, i.e., the disk is gravitationally stable for an axisymmetric mode, the effective value, $Q_{\rm eff}$, becomes much less than unity after a few Myr due to the thermal instability (see Fig. 3 in Paper I). The term $Q_{\rm eff}$ is defined as $Q_{\rm eff}(R) \equiv \kappa\sigma_v/\pi G\Sigma_g$, where κ is the epicyclic frequency. Azimuthally averaged ($\Delta R =$ 20 pc) velocity dispersion σ_v is defined by $\sigma_v \equiv (\langle v^2 \rangle_{\Delta R} - \langle v \rangle_{\Delta R}^2)^{1/2}$ with $v \equiv |\boldsymbol{v}| + c_s$, where $\boldsymbol{v}$ the flow velocity and c_s is the sound velocity of the gas. The gas temperature decreases from the initial value ($\sim 10^4$ K) to an equilibrium temperature ($\sim 10^2$ K) within 10^5 yr. Since the initial density is higher in the central region of the disk than in the outer region, gravitational instabilities begin in the inner few 100 pc and develop outward. The gravitational instability goes into the nonlinear regime in the inner region at $t \sim 2$ Myr. We can see spatial fluctuations in temperature at $t = 2$ Myr. The density fluctuations evolve nonlinearly from inside to out, and many dense filaments and clumps are formed. Such clumps tidally interact and filamentary tails are produced. Filaments and clumps are merged to produce more massive structure, and finally a complicated network of many filaments is formed. The temperature fluctuations also evolve and high-temperature gas ($T \sim 10^5$ K) appears after $t = 6$ Myr.

At $t = 10$ Myr, gravitational instabilities over the whole of central 500 pc are in the nonlinear phase, where the maximum density contrast is about 10^6. At $t = 25$ Myr, the instability grows nonlinearly over the whole of the disk and forms meshlike structure consisting of many clumps, filaments, and low-density voids (see Fig. 1 in Paper I). As a result, a globally stable multiphase structure is formed in which high-temperature, low-density gas and low-temperature, high-density phases coexist. The density range is from 10^{-1} to 10^6 $M_\odot$ pc^{-2}, which corresponds to about 0.03–3 × 10^5 cm^{-3}. The size of the highest density clouds is about 5–50 pc, although they are not necessarily round in shape. The high-density clumps are embedded in filamentary structure; in other words, they are not isolated. Their density is about 10^3–10^6 $M_\odot$ pc^{-2} and the temperature is less than 100 K.

The temperature of the low-density gas in the voids sometimes reaches 10^5–10^6 K. This is due to shock heating, and the energy source is turbulent-like random motion of the gas, which reaches ~ 100 km s^{-1} locally. The origin of the random motion is the galactic rotation (i.e., stellar and dark matter potential) and the self-gravity of the gas.

Although the global spiral-like enhancements can be seen in the pressure map (Fig. 7*a*), the small-scale filamentary structure in the density map is less prominent in the pressure map. This means that the filaments are in pressure equilibrium with their ambient gas. This equilibrium, however, is satisfied only over a local scale (< 100 pc). The pressure over the simulated region (2 × 2 kpc) changes by of order 10^3–10^6. However, the filamentary structure is still seen in the map, especially in the regions between the spiral-like enhancements, which means that they are not in thermal pressure equilibrium with the ambient diffuse gas.

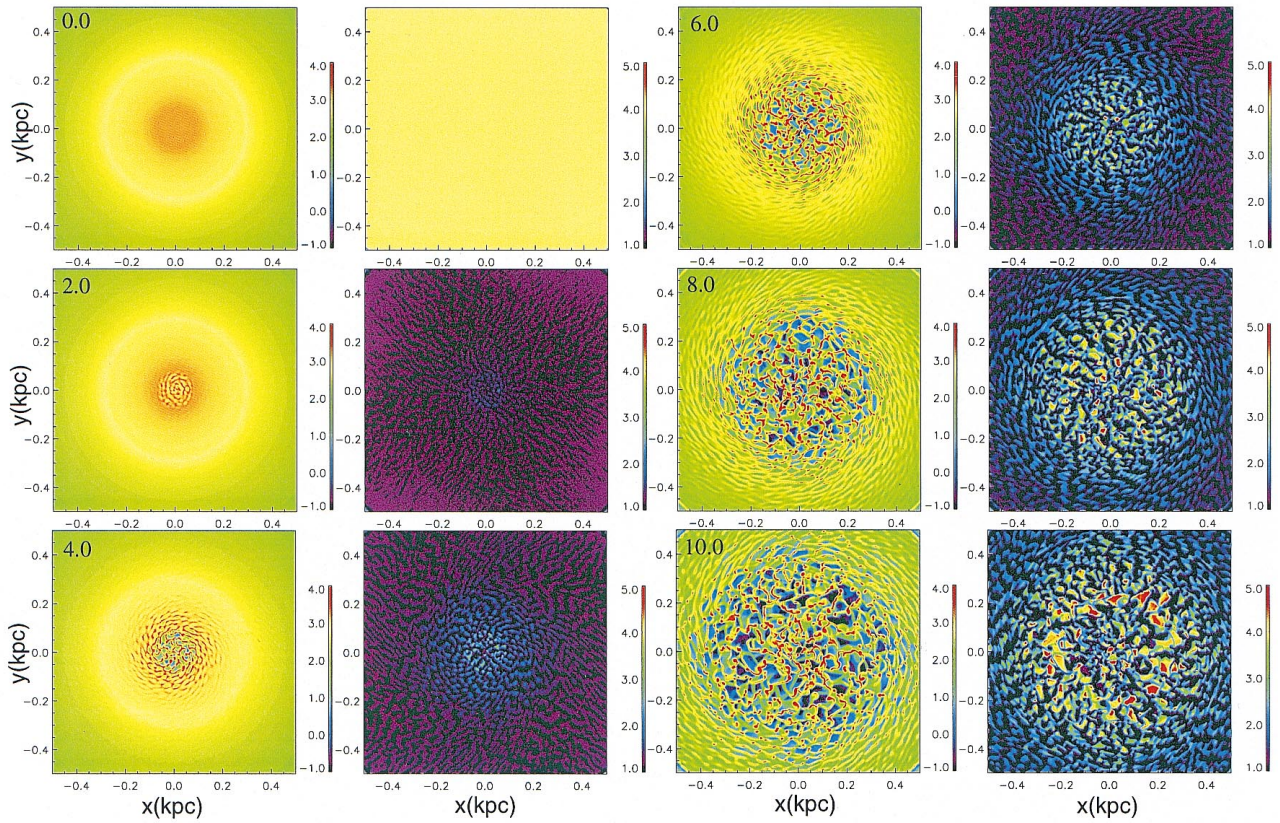

FIG. 6.—Initial 10 Myr evolution of a model without stellar energy feedback (model NSF). Surface density (*first and third rows*) and temperature distribution (*second and forth rows*) in the central 1 × 1 kpc are shown. The color represents log-scaled surface density and temperature of the gas, and their units are $M_\odot$ pc^{-2} and K, respectively. Time is shown at the upper left corners of the density panels in a units of Myr. The rotational period at $R = 200$ pc is about 8 Myr. The density and temperature fluctuations evolve from a linear stage to a nonlinear stage, and a complicated network of many filaments is formed in 10 Myr.

In Figure 7*b* the vorticity distribution is plotted for the same model and region of Figure 7*a*. This is surprisingly rich in structure. The maximum and minimum vorticity in this map are ± 40 km s^{-1} pc^{-1}. Comparing the density and temperature distributions and the pressure distribution, we find that high-pressure regions ($P/k_B \sim 10^5$ cm^{-3}) can be categorized into three regimes: (1) high density and low-temperature clumps ($\Sigma_g \sim 10^5$ $M_\odot$ pc^{-2}), (2) low-density

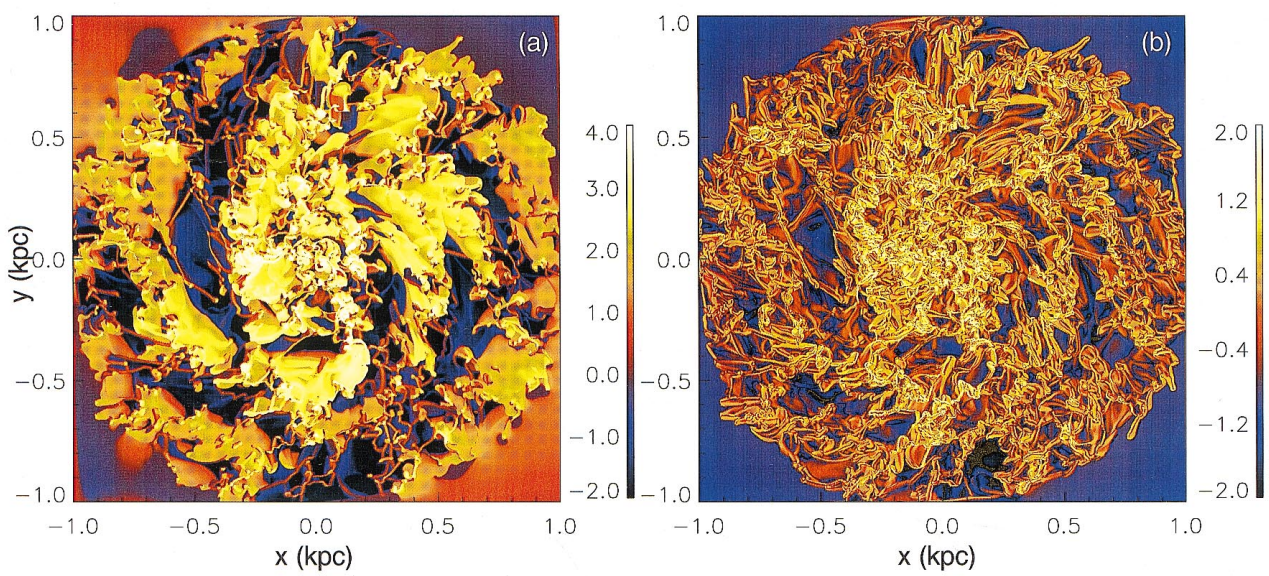

FIG. 7.—Log-scaled distributions of thermal pressure, $p_{\rm th}/k_B = \Sigma_g T_g$ ($M_\odot$ pc^{-2} K), and vorticity, $\nabla \times \boldsymbol{v}$ (km s^{-2} pc^{-1}), where $\boldsymbol{v}$ is the local velocity field, of the model NSF at $t = 50$ Myr.

high-temperature voids, and (3) intermediate-density ($\Sigma_g \sim 10^1$–$10^2\ M_\odot\ \mathrm{pc}^{-2}$) and $T \sim 10^4$ K. The regime 2 or 3 roughly coincides with the high vorticity region. This can be interpreted as thermalization of the gas in the turbulent region. There are strong local shear motions associated with the filaments. Oblique shocks also cause the high vorticity.

Figure 8 shows the time evolution of gas mass for five temperature ranges (regime 1: $T_g < 100$ K, regime 2: $100\ K < T_g < 9000$ K, regime 3: $9000 < T_g < 11{,}000$ K, regime 4: $11{,}000 < KT_g < 10^5$ K, and regime 5: $T_g \geq 10^5$ K). The five regimes are determined in order to represent the thermally critical temperature ($T_g \sim 100$, $\sim 10^4$, and $\sim 10^5$ K; see Fig. 1). Regime 3 is for the fraction of the gas around 10^4 K gas, because it is the most dominant phase in a model without stellar energy feedback (Wada & Norman 1999). The total gas mass is $6 \times 10^8\ M_\odot$. The fraction of each component does not change so much after ~ 30 Myr. It shows that about 80% of the mass is in the cold phase of regime 1. In other words, the cold and dense clumps dominate the total gas mass. The second dominant phase is regime 2 gas. In this phase, most gas forms clumps or filaments, which are seen in blue or green in the temperature map (Fig. 6). As seen in Figure 8, the mass of this warm gas (regime 2) increases from 10^7 to $10^8\ M_\odot$ in the first 10 Myr. It is notable that the gas mass in regimes 4 and 5 increases by a factor of 100 for the first 30 Myr. In the quasi-stable phase, the relatively hot gases of regimes 4 and 5 occupy about 0.3% of the total mass. The volume filling factor shown for each regimes in Figure 9 indicates that the hot gases (regime 4 and 5) occupy a few hundred times larger volume than the cold gas of regime 1. The volume filling factor of the gas in regime 4 increases from 0% to $\sim 30\%$ until $T = 30$ Myr, and the cold gas fraction in regime 1 decreases from 48% to 10% in the same period. After 30 Myr from the start of the calculation, the volume filling factors reach a global quasi-equilibrium state.

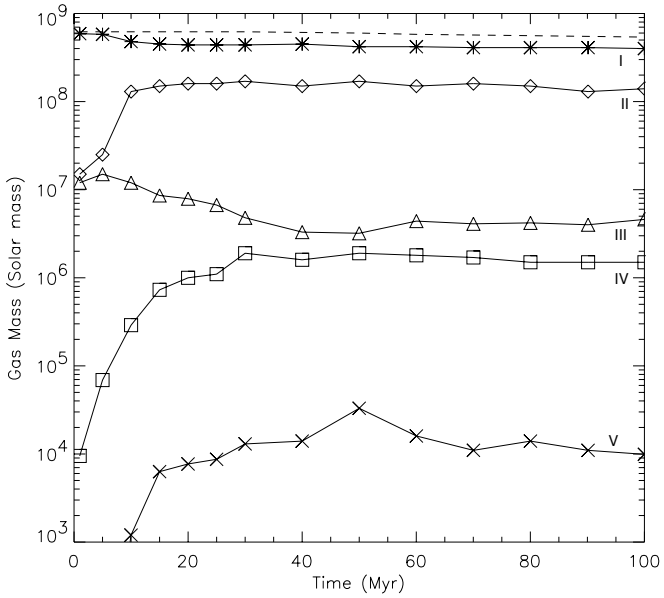

FIG. 8.—Time evolution of gas masses for five temperature regimes; regime 1: $T_g < 100$ K (*asterisks*), regime 2: 100 K $< T <$ 9000 K (*diamonds*), regime 3: 9000 K $< T <$ 11,000 K (*triangles*), Regime 4: 11,000 K $< T < 10^5$ K (*squares*), and regime 5: $T \geq 10^5$ K (*crosses*). The dashed line represents the total gas mass ($6 \times 10^8\ M_\odot\ \mathrm{pc}^{-2}$), which is dominated by the cold gas (regime 1). The shock-heated hot gases in regimes 4 and 5 become prominent in the initial 40 Myr.

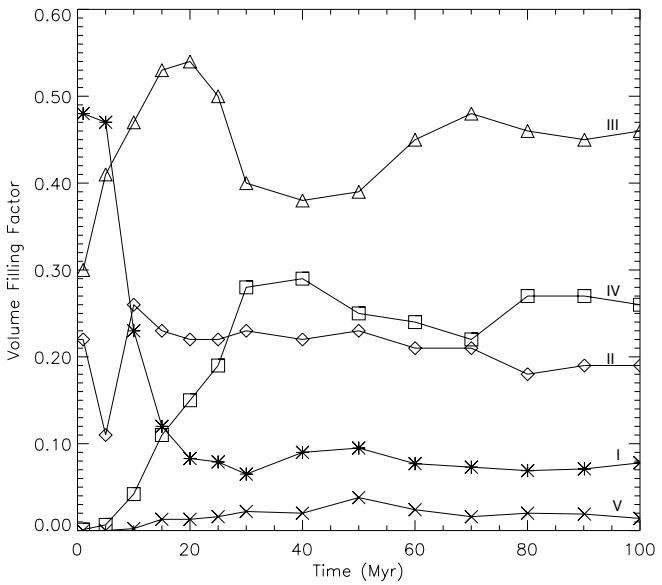

FIG. 9.—Same as Fig. 8, but for the volume filling factors for the five regimes. In contrast to Fig. 8, the cold gas (regime 1: $T_g < 100$ K; *stars*) occupies 8% of the volume.

Figure 10 is evolution of total "entropy" $[\sum_{i,j} (p/\Sigma_g^{\gamma-1})_{i,j}]$ (Ryu et al. 1993) for models without stellar energy feedback. If $\sum_{i,j} (p/\Sigma_g^{\gamma-1})_{i,j} =$ constant, it means that the system is globally in a thermal equilibrium state. The total "entropy" increases very rapidly in the first 20 Myr, and it stays roughly constant after 70 Myr. This plot shows the gas disk is heated due to shocks, and again the global system reaches a quasi-equilibrium after about one rotation period.

One should note, however, that the globally stable state does not mean that the local filamentary and porous structure whose scale is less than 1 kpc is also in a stable state. On such small scales, the ISM is both dynamic and tran-

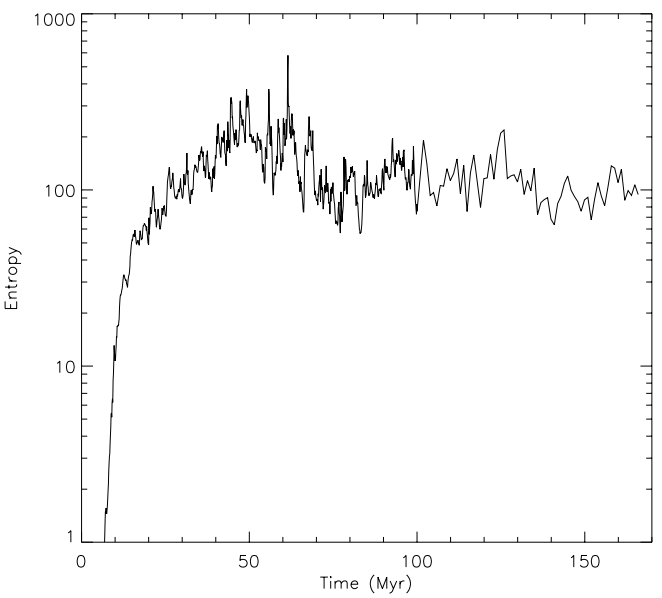

FIG. 10.—Evolution of total "entropy," $\sum_{i,j} (p_{\mathrm{th}}/\Sigma_g^{\gamma-1})_{i,j}$, where $\sum_{i,j}$ means the sum for the grid points (i, j), for the model without stellar energy feedback (model NSF). The data is plotted every 0.1 Myr ($t < 100$ Myr) and 1.0 Myr ($t > 100$ Myr). This plot shows that the system is heated up in the initial $\sim$ 50 Myr and then stays in a quasi-equilibrium state in a global sense.

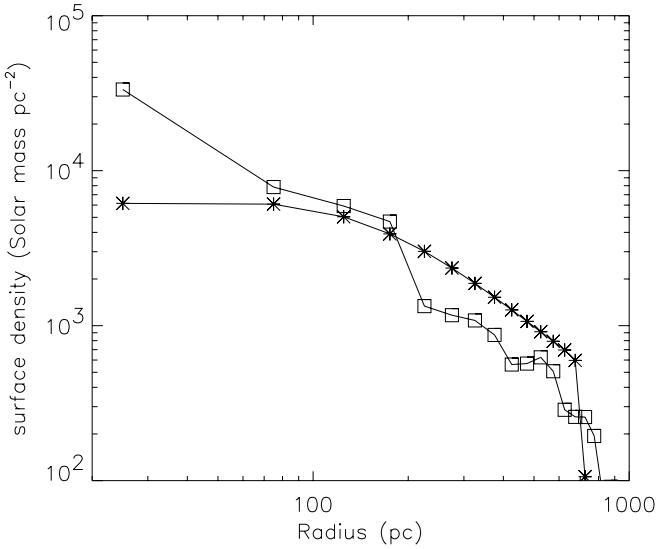

FIG. 11.—Radial surface density distribution of the model NSF at $t = 0$ Myr (*asterisks*) and at $t = 100$ Myr (*open squares*).

sient, which is similar to the previous local models of the turbulent ISM (Vázquez-Semadeni et al. 1995; Passot et al. 1995; Gazol-Patino & Passot 1999).

In Figure 11, we plot the radial surface density distribution of the model NSF at $t = 0$ Myr and at $t = 100$ Myr. The initial exponential profile changes to the power-law–like distribution, and the gas density inside $R = 200$ pc increases by a factor of ~ 1.2–2. This evolution implies that there is inflow of the mass and outflow of the angular momentum in the system, which are caused by the kinematic viscosity due to the random motion in the inhomogeneous gas disk. Since the velocity dispersion of the turbulent-like system, σ_v, is an order of 10 km s^{-1} and the typical scale of the vortices, l_v, is $l_v \sim 100$ pc (see Fig. 7*b* and Fig. 18), the effective viscosity, $\nu_{\rm eff}$, is $\nu_{\rm eff} \sim \sigma_v l_v \sim 10^3$ pc^2 Myr^{-1}. Therefore the viscous timescale, τ_v, for $R \sim 100$ or 1000 pc would be $\tau_v \sim R^2/\nu_{\rm eff} \sim 10^7$ yr or 10^9 yr. Figure 11 suggests that the density distribution of the system changes in a timescale of $\sim 10^8$ yr, and this is consistent with above estimate.

We find that the multiphase, globally quasi-stable ISM is formed from a highly gravitationally and thermally unstable state on a local scale. The resultant structure is naturally porous, i.e., low-density gases occupy large volumes, and dense gases dominate the total gas mass. Shock heating is a dominant internal heating mechanism in this system. Differential rotation of the disk and gravitational perturbations from clumps are the main energy source for the shock heating.

4.2. *Structure of a Multiphase Disk with Energy Feedback*

Figure 12 shows density and temperature maps at $t = 150$ Myr for a model with stellar energy feedback (model SF). One can compare these maps with Figure 1 of Paper I, which is a result of a model without energy feedback. Their morphology looks similar, but note that in the temperature map (Fig. 12), the maximum temperature reaches 10^7 K, whereas it reaches 10^5 K in Figure 1 of Paper I. The hot gases ($T_g > 10^6$ K) are produced by SNe mostly inside $R = 1$ kpc. Relatively old SNRs can be recognized as the yellow regions ($T_g \sim 10^6$ K) at $R \gtrsim 500$ pc. In contrast to supernova remnants in a uniform and stationary media, the remnants in the present model are not axisymmetric. Similarly to the model NSF discussed above, the structure of the model SF is also characterized by a complicated network of high-density filaments, many clumps, and low-density voids. It is notable that a global spiral-like density enhancement, which is roughly four-armed, is produced. The global spiral arms are not smoothed waves, but they are formed from many short filaments and clumps. This is very similar to the fine structure of the dust lanes of spiral galaxies, which has been recently revealed by *HST* (Colina & Wada 2000).

The multiphase structure of the gas is clearly shown in Figure 13, which is a phase diagram consisting of a contour plot of volume in a surface density versus pressure plane. The two plots are Σ_g-$p_{\rm th}$ and Σ_g-$p_{\rm eff}$ of model SF at $t = 115$ Myr, respectively, where $p_{\rm th}$ is the thermal pressure and the effective pressure, $p_{\rm eff} = p_{\rm th} + C\Sigma_g \sigma_g^2$, C is a constant, and

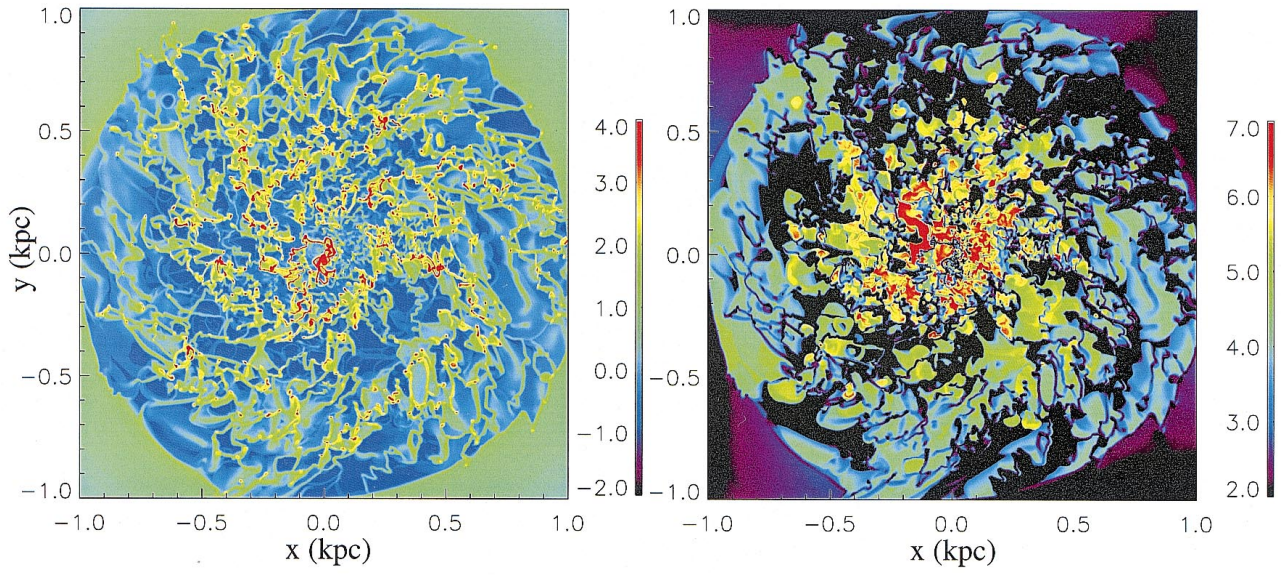

FIG. 12.—Density (*left*) and temperature (*right*) maps at $t = 150$ Myr of a model with stellar energy feedback (model SF). The color bar is log scale. The density range is 10^{-1} to 10^5 $M_\odot$ pc^{-2}, and temperature range is 10–10^8 K.

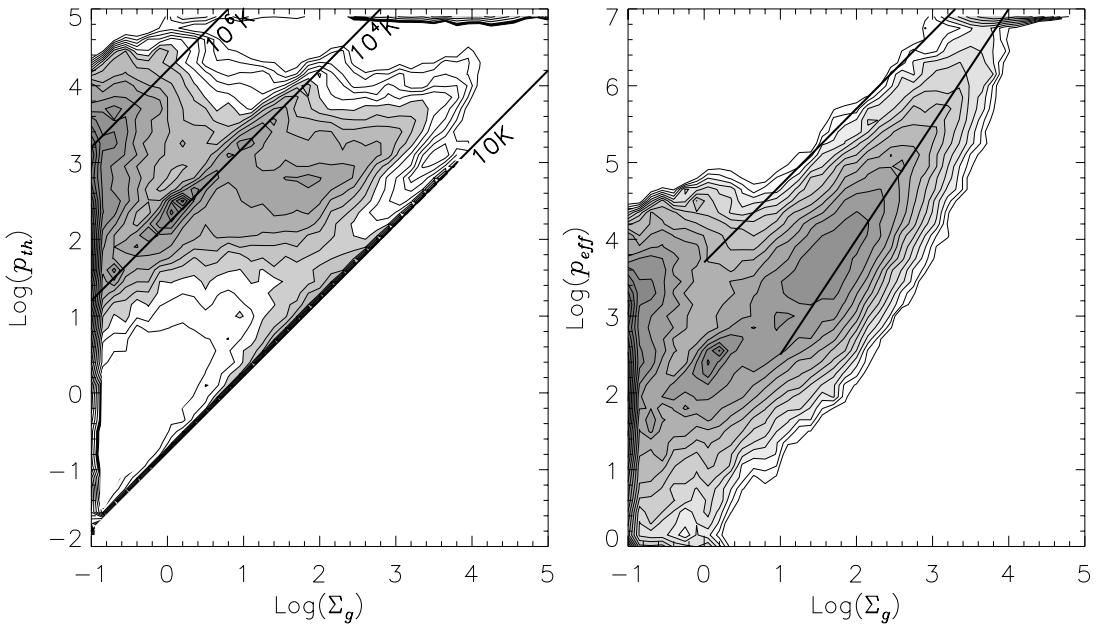

FIG. 13.—Two-dimensional histograms for pressure ($M_\odot$ pc^{-2} K) and surface density ($M_\odot$ pc^{-2}) (phase diagrams) of model SF at $t = 115$ Myr. The left panel is Σ_g-$p_{\rm th}$, and the right panel is Σ_g-$p_{\rm eff}$, where $p_{\rm th}$ is the thermal pressure and the effective pressure $p_{\rm eff} = p_{\rm th} + C\Sigma_g \sigma_g^2$. The contours represent log-scaled number of grid points, and they are drawn every $10^{0.25}$ between $10^{1.5}$ and 10^4. The larger value is more deeply hatched. Three diagonal lines in the left panel represent the gaseous temperatures $T_g = 10^6$, 10^4, and 10 K. The two thick lines in the right-hand panel represent $p_{\rm eff} \propto \Sigma_g$ and $p_{\rm eff} \propto \Sigma_g^{1.5}$.

σ_g is mean velocity dispersion, which is defined by $\sigma_g \equiv [(\langle |\boldsymbol{v}|^2 \rangle - \langle |\boldsymbol{v}| \rangle^2)]^{1/2}$, where $\langle \boldsymbol{v} \rangle$ means averaging the gaseous local velocity field, $\boldsymbol{v}$, over a 100 pc scale. Note that the vertical range in the two panels are different. The hot, diffuse gas ($T_g > 10^6$ K and $\Sigma_g < 1\ M_\odot$ pc^{-2}) is prominent in the left-hand panel of Figure 13 and is not observed in a model without SNe (see Fig. 2 in Paper I). One can see three major isothermal components at $T_g \sim 10^6$, 10^4, and 10^2 K in the Σ_g-$p_{\rm th}$ diagram. The coldest component around $T_g \sim 10$ K is not prominent in this diagram because such cold gas occupies a very small volume (Fig. 9). The three-phase ISM model has been discussed in many theoretical studies (e.g., McKee & Ostriker 1977). However, one should note that the three phases are *not* the only components of the multiphase ISM, but the ISM is rather smoothly distributed between $T_g = 10$ and $T_g = 10^7$ K (cf. Norman & Ferrara 1996). The right-hand panel of Figure 13, on the other hand, implies that the turbulent pressure dominates the thermal pressure especially for dense gas ($\Sigma_g > 10\ M_\odot$ pc^{-2}). Most dense gases follow the single distribution around $p_{\rm eff} \propto \Sigma_g^{1.5}$. Since $p_{\rm eff} \sim G\Sigma_g^2 L$, where L is a typical scale length, if the dense gas is formed through a mass conservation process ($\Sigma_g \propto L^{-2}$), such as shock compression, one can expect that $p_{\rm eff} \propto G\Sigma_g^{1.5}$. The upper boundary for $\Sigma_g > 10\ M_\odot$ pc^{-2} is $p_{\rm eff} \propto \Sigma_g$, which corresponds to a maximum velocity dispersion that is roughly constant, ~ 50 km s^{-1}, independent of Σ_g.

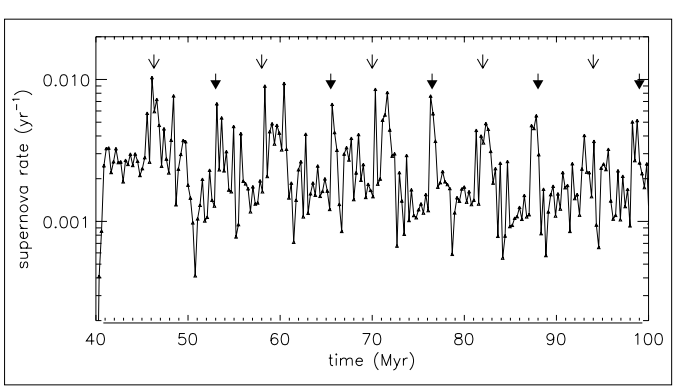

FIG. 14.—Evolution of the total supernova rate (yr^{-1}) of a model with stellar energy feedback (model SF). The many peaks are many recurrent bursts of SNe. Two *causal* groups, as examples, are shown by two types of arrows (see § 4.2).

We find that the total supernova rate in the central 1 kpc region of model SF is time dependent, and it varies by a factor of 10 (0.001–0.01 yr^{-1}) during 6×10^7 yr (Fig. 14). This supernova rate per unit area is about 10–100 times larger than the average value in our Galaxy, and it is 1/30–1/3 of the value in starburst galaxies, such as M82 (Bregman, Temi, & Rank 2000). The behavior seems to be chaotic, but actually these peaks consist of many *causal* groups of recurrent bursts, in which each time interval is about 10 Myr. For example, we show two causal groups by two types of the arrows in Figure 14. The reason for the recurrent bursts is simple. A burst of supernovae generate many strong shocks that propagate toward the ambient gas, and they compress clouds or filaments, where the star formation criterion (§ 2.3) was not satisfied before the bursts. As a result, new massive stars are born in the clouds or filaments. These *second-generation* stars eventually explode somewhere as supernovae after about 10 Myr, then again new star formation is triggered. Therefore recurrent bursts naturally appear, once the initial burst happens. This result implies that a burst of star formation could originate in a triggering event $\sim 10^8$ yr ago.

5. STATISTICAL PROPERTIES OF THE MULTIPHASE ISM

As we described in the previous section, the morphology and dynamics of the multiphase ISM are extremely complex. However, we find that the medium has simple statistical properties, even if stellar energy feedback is included. Here we focus on the probability density function,

which represents the density structure of the medium, and on the energy spectra, which elucidates the kinematical nature of the turbulent medium.

5.1. *Probability Density Function*

Probability density functions (pdf's) have been discussed in relation to the structure of the turbulent interstellar medium (ISM) and the stellar initial mass function (Vázquez-Semadeni 1994; Padoan, Nordlund, & Jones 1997; Scalo et al. 1998; Nordlund & Padoan 1998; Passot & Vázquez-Semadeni 1998). Vázquez-Semadeni (1994) reported lognormal pdf's in his two-dimensional isothermal turbulent simulations. Scalo et al. (1998) showed power-law pdf's in their numerical simulations of two-dimensional self-gravitating supersonic magnetohydrodynamic turbulence. Based on their two-dimensional simulations of Burgers' turbulence, they suggested that a power-law shape of the pdf is the signature of the nonlinear advection operator. They also pointed out that the pdf is lognormal only for effective polytropic indices of $\gamma \sim 1$ (i.e., isothermal), from results of their one-dimensional simulations of forced supersonic polytropic turbulence. Nordlund & Padoan (1998) indicated a formal proof for the lognormal pdf in isothermal supersonic turbulence and also showed numerically that the lognormal pdf appears in three-dimensional isothermal supersonic turbulence. They claimed that the pdf's are skewed if the adiabatic index $\gamma < 1$, but the difference was less than a factor of 2 from a lognormal pdf. However, the density range discussed in these studies is less than 4 orders of magnitude. Moreover, the density range that can be fitted by a power-law pdf (Scalo et al. 1998) is only over 1 or 2 orders of magnitude. Gravitational instability, which is crucial to produce the high densities, is not followed with sufficient detail, because self-gravity of the gas was ignored in these prior simulations. In addition, previous numerical simulations on turbulence assumed uniform turbulence with periodic boundaries. Clearly, the real ISM in galaxies is not a uniform, turbulent medium. In this section, we report on pdf's in the global model of a stable multiphase ISM models, shown in § 4.

One of the remarkable results we have found on the structure of the multiphase ISM in a quasi-steady state is the following: *The pdf has a lognormal profile over 4 orders of magnitude ranging over 7 orders of magnitude in density.* Here the density pdf is defined as the number of grid points whose density is in a given density range. It is clear in Figure 15 that the pdf of the model without star formation is perfectly fitted by a single lognormal function, its average density is $10^{2.2}\ M_\odot\ \mathrm{pc}^{-2}$, and the dispersion is $10^{1.4}\ M_\odot\ \mathrm{pc}^{-2}$, for $\Sigma_g = 10^2$–$10^6\ M_\odot\ \mathrm{pc}^{-2}$.

Figure 16 shows the pdf's for the central $(400\ \mathrm{pc})^2$ region for the models with and without star formation. The star formation and supernovae are most active in this region of the star formation models where the maximum supernova rate is about $0.01\ \mathrm{yr}^{-1}$. In spite of many supernova explosions, the entire shape of the pdf is similar to that in models without star formation. In fact, as noted above, the filamentary and clumpy multiphase structure is similar in both the non–star-forming and star-forming models (see Fig. 12 and Fig. 1 in Paper I). The pdf for the model with star formation also shows the lognormal profile, but its dispersion is larger than that in the non–star-forming model. This result is consistent with Passot & Vázquez-Semadeni (1998), in which the authors claimed that the lognormal pdf depends on rms

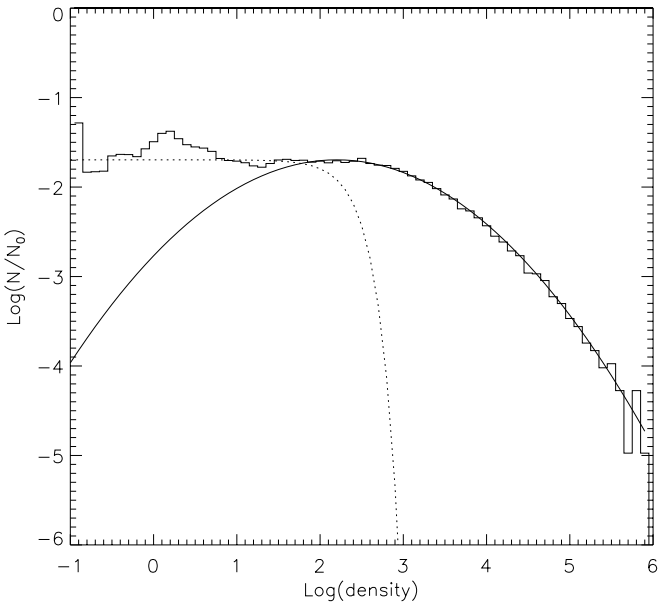

FIG. 15.—One-point probability density function (pdf) of model NSF at $t = 166$ Myr. The solid and dotted curves represent lognormal and normal functions. The pdf for the dense part is perfectly fitted by a single lognormal function; its average density is $10^{2.2}\ M_\odot\ \mathrm{pc}^{-2}$ and the dispersion is $10^{1.41}\ M_\odot\ \mathrm{pc}^{-2}$.

Mach number. The pdf shows a power-law tail ($\propto \Sigma_g^{0.8}$) for the high-density region ($\Sigma_g > 10^5\ M_\odot\ \mathrm{pc}^{-2}$) rather than the lognormal distribution. However, while intriguing, this is not yet a statistically definite conclusion, because only several tens of cells contribute to the "power-law" tail.

The lognormal part of the pdf implies hierarchical structure caused by nonlinear evolution of the dense region or, in other words, a succession of many probabilistic steps (see Vázquez-Semadeni 1994). In our case, the high-density

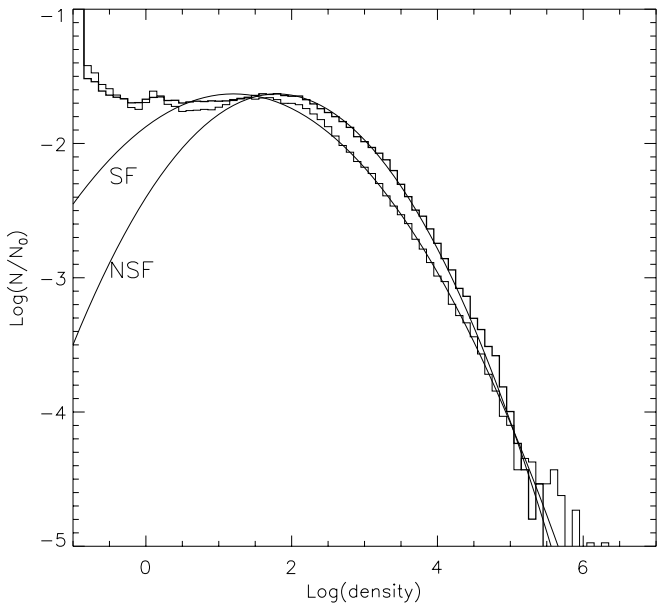

FIG. 16.—The pdf's for the central $(400\ \mathrm{pc})^2$ region for the models with star formation (SF) and without star formation (NSF). Both pdf's in the dense part are well fitted by the lognormal functions (*thick and thin solid curves*).

clumps are formed in a gravitational instability in lower density filaments, or collision between the filaments or shocks. The pdf for low-density cavities is rather a *normal* distribution than a *lognormal* distribution. The flat pdf's are not observed in previous simulations of turbulent media. However, the flat pdf in the low-density region ($\Sigma_g < 100$ $M_\odot$ pc^{-2}) may indicate that the formation mechanism has a different physical origin from the lognormal part (see also § 6).

It is significant that the timescale to set up the lognormal and normal distributions is very short, of order 12 Myr, which is local dynamical timescale. Figure 17 is the initial 10 Myr evolution of the pdf in model NSF. As we see, the normal part low-density part evolves very rapidly, and simultaneously the lognormal part ($\Sigma_g > 10^3$ $M_\odot$ pc^{-2}) appears.

The origin of the lognormal distribution calculated here is different from previous work. There is no need for an isothermal equation of state which we regard as a very special case that can generate a lognormal pdf in the absence of self-gravity.

5.2. *Energy Spectrum*

The energy spectrum is useful to represent kinematical properties of the turbulent medium. Numerical experiments of compressible, hydrodynamic turbulence show power-law behavior of the energy spectrum (Dahlburg et al. 1990; Vázquez-Semadeni et al. 1996), where the spectral index is close to -3, which corresponds to a direct cascade of enstrophy (mean squared vorticity) (Kraichnan 1967). In contrast to these numerical experiments, our global model of the ISM presents examples of highly compressible turbulence in more realistic situations. We divide the turbulent velocity field $\boldsymbol{v}_{\rm tub} \equiv \boldsymbol{v} - \langle \boldsymbol{v}_c \rangle$, where $\langle \boldsymbol{v}_c \rangle$ is the mean circular rotational velocity, into two components, i.e., $\boldsymbol{v}_{\rm tub} = \boldsymbol{v}_{\rm comp} + \boldsymbol{v}_{\rm sol}$, where $\boldsymbol{v}_{\rm comp}$ is the compressible or rotation free velocity field and $\boldsymbol{v}_{\rm sol}$ is the incompressible or solenoidal one. The two components are defined as $\nabla \cdot \boldsymbol{v}_{\rm tub} = \nabla \cdot \boldsymbol{v}_{\rm comp}$ and $\nabla \times \boldsymbol{v} = \nabla_{\rm tub} \times \boldsymbol{v}_{\rm sol}$. We plot the spectra of the compressible and incompressible velocity fields of model NSF and SF in Figures 18*a* and 18*b*. Their power-law behavior indicates that the velocity field of our model is turbulent-like. In both models, the amplitude of incompressible (solenoidal) and compressible components are comparable, except for small wavenumber ($k < 10$). The spectral index is, however, different between the models: $E(k) \propto k^{-3}$ between $k = 20$ and 200 for model NSF and k^{-2} between $k = 20$ and 100 for model SF. The spectral index of model NSF is consistent with that of Vázquez-Semadeni et al. (1995) in a non–star-forming epoch. This result is consistent with Kraichnan's prediction, of an inverse cascade of energy with respect to enstrophy, and the typical scale of the forcing is ~ 200 pc in our case. On the other hand, the -2 index of the star-forming model means that shocks dominate the

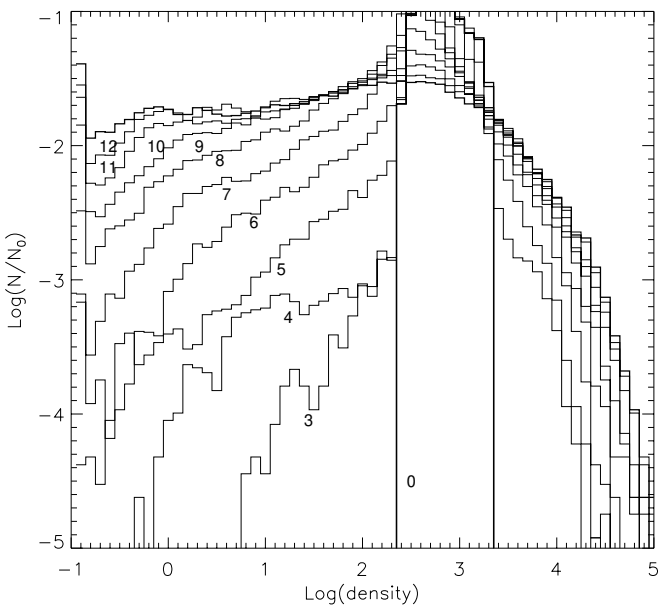

FIG. 17.—Evolution of the density pdf of model NSF. The thick lines are the pdf at $t = 0$ and $t = 12$, and the pdf's from $t = 3$ to $t = 11$ Myr are plotted at intervals of 1 Myr. The lognormal and normal pdf's are achieved simultaneously in the local dynamical timescale, ~ 10 Myr.

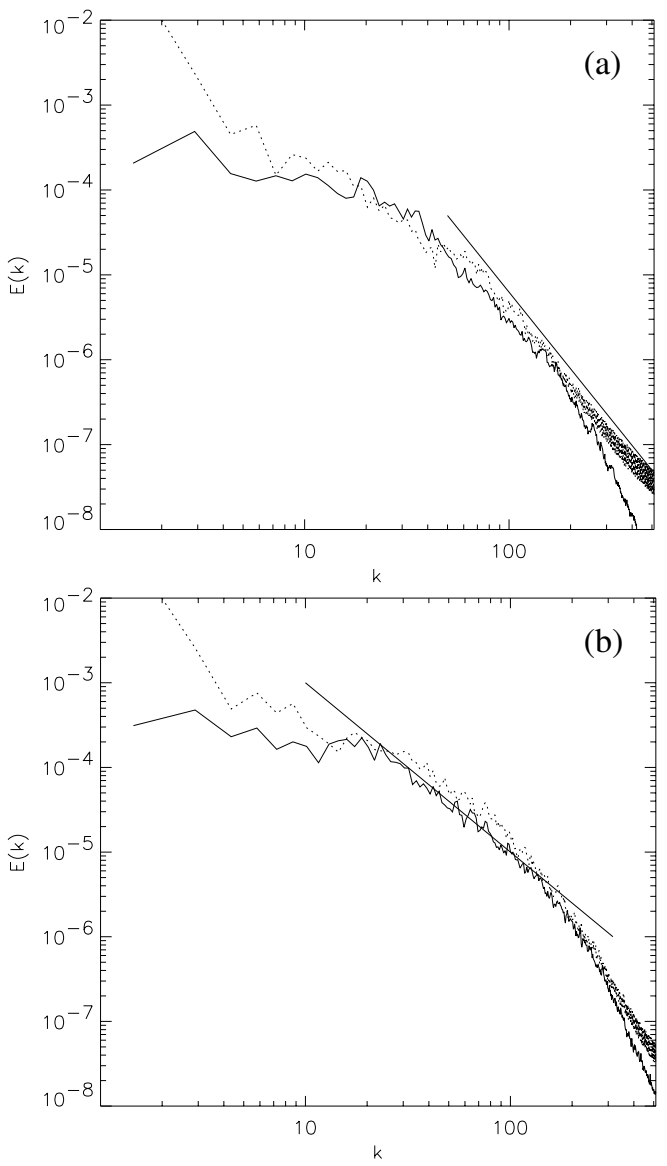

FIG. 18.—Energy spectra, $E(k)$, of the local velocity field as a function of wavenumber, k, of models (*a*) NSF and (*b*) SF. Thick solid line and dotted line are energy spectra for compressible (rotation free) and incompressible (solenoidal) velocity fields. Thin solid lines represent power-law slopes of (*a*) $E(k) \propto k^{-3}$ and (*b*) $E(k) \propto k^{-2}$.

system over a scale of $l \sim 20$–100 pc, which is the typical scale of shocks due to supernovae. This result is consistent with the local simulations of a turbulent medium by Passot, Pouquet, & Woodward (1988). In conclusion, the global ISM shows turbulent-like behavior, and smaller scale vortices have more power if stellar energy feedback dominates the system. The energy sources of the turbulence in this system originate in the shear driven by galactic rotation, the self-gravitational energy of the gas, and the stellar energy feedback in model SF. We do not have to introduce nonrealistic external forcing fields to maintain the turbulence, as is often the case in numerical simulations of turbulence.

6. DISCUSSION

We have shown that a globally stable multiphase ISM with feedback from stellar winds and supernovae is formed as a natural consequence of the nonlinear evolution of a self-gravitating gas disk.

In spite of such complexity, it is remarkable that the density probability function for dense regions can be fitted by a simple lognormal pdf over 5 orders of magnitude, and the void regions can be fitted by the normal pdf. Star formation activity does not change the lognormal pdf, but its dispersion becomes larger. It is obvious that these results on pdf's may have important implications for a number of associated issues in galaxy research including the mass spectrum of molecular clouds in galaxies, the initial mass function, and the turbulent source functions in the central regions of spiral galaxies. The mass spectrum of molecular clouds and its origin have been discussed extensively (e.g., Larson 1981). The spectrum includes some information about the spatial structure of the dense interstellar gas. However, the spectrum of clouds would change its shape depending on the definition and identification of clouds. Moreover the spectrum is usually noisy, so it is not easy to discuss its physical background (see Fig. 8 in Wada, Spaans, & Kim 2000). On the other hand, our results show that a probability density function for the dense gas component can be represented over a wide range by a simple and robust function and imply that there is an underlying physical or statistical reason for this distribution.

Vázquez-Semadeni, Gazol, & Scalo (2000, hereafter VGS) have investigated numerically the role of thermal instability in the context of a globally turbulent medium. Their two-dimensional, local simulations of the ISM include the magnetic field, the Coriolis force, self-gravity, and stellar energy injection. They found that combination of the stellar forcing and the effective pressure provided by the magnetic field and the Coriolis force overwhelm the thermal instability as a density-structure generator in the ISM. This result is consistent with ours, namely, the structure of the ISM is determined not only by the thermal instability but also by the dynamics of the self-gravitating, compressible medium and stellar energy feedback. However their pdf for the ISM-like simulations (see Fig. 11 in VGS) looks different from our lognormal-normal pdf. One should note that the density ranges in our pdf and theirs are significantly different: 7 orders of magnitude in ours and 2 orders of magnitude in theirs. This difference would be mainly caused by the difference of the numerical schemes. The spectral scheme they used cannot handle very strong shocks, and therefore the simulations must be stopped when the density gradients of the physical variables become too steep (see § 2 in VGS). The VGS simulations do not reach the highly nonlinear stage achieved in our simulations. In addition to this, their local simulations with 128^2 grid points do not seem to have a statistically sufficient number of sampling points, although their pdf's are averaged over several time steps to improve the statistics. Therefore it is not straightforward to make a comparison of pdf's between these simulations.

The two types of the pdf's, i.e., lognormal and normal (§ 5.1), would imply that the physics that dominates in the structural formation is different between dense and less dense parts. However, they might be unified to a single Lévy distribution function,

$$p(x) = \frac{1}{2\pi} \int_{-\infty}^{\infty} \exp(-ikx) \exp(-|k|^{\alpha}) dk , \qquad (21)$$

where α is a constant in a range $0 < \alpha < 2$. The Lévy distribution appears for the distributions of sums in independent random variables. It becomes the normal distribution function when $\alpha = 2$. For small α it can be represented as the sum of a normal and lognormal distribution (Montroll & Bendler 1984; Montroll & Shlesinger 1983). The pdf may be represented by the single Lévy distribution and would then imply that the diffuse and dense regions are formed by the same highly nonlinear process, which is statistically identical to sums of many independent random variables.

The origin of supergiant H I holes in galaxies has been controversial (see also Walter & Brinks 1999). If the observed kiloparsec-scale holes and shells are caused by explosional phenomena only, one needs highly energetic events. However, our numerical simulations give an alternative explanation of the origin of the large-scale holes: the nonlinear evolution of the multiphase gas disk. In the multiphase ISM, most of the gas mass is concentrated in the cold, dense clumps and filaments, but the volume filling factor of such dense component is much smaller than that of the hot diffuse gas. Therefore the multiphase ISM in a quasi-steady state is naturally porous. Our results suggest that if the energy feedback from massive stars are not effective, kiloparsec-scale inhomogeneities can evolve in a disk in $\sim 10^8$ yr. Dense filaments can change shape due to local random velocity fields as well as the global shear and often show kinematic features similar to those of expanding shells (Wada, Spaans, & Kim 2000). We suspect that a significant number of supergiant holes and shells in dwarf galaxies may not have an explosive origin. Deul & den Hartog (1990) interpreted the large number of regions that are devoid of H I emission in M33 as holes formed by interstellar winds. They shows that small ($D < 200$ pc) H I holes correlate well with OB associations, but large ($D > 500$ pc) holes show an anticorrelation, in the sense that the H II regions and OB associations lie on the hole edge. This is consistent with our results. The small-scale holes could be of stellar origin, but the large-scale ones are results of nonlinear evolution of the gas disk. We suspect that the H II regions and OB associations on the hole edge are not the direct results of explosions in the holes, but they would be secondary products in the inhomogeneous ISM. We believe, based on our simulations, that many cavities in the ISM that create the porosity structure are a natural consequence of nonlinear evolution of the multiphase ISM. The supernovae explosions do form small cavities filled with hot gases ($T_g > 10^7$ K), but they may not be the only major contributor to form a large-scale (>100 pc) low-density region. Rather, they prevent large cavities from forming (Wada, Spaans, & Kim 2000).

We have shown in § 4.2 that recurrent bursts of star formation are a natural consequence of energy feedback from supernovae in the multiphase interstellar medium. This suggests that if one observes starbursts in a galaxy, it does not mean that a triggering event, such as a galaxy-galaxy encounter, or minor merger is ongoing. One triggering event causes a burst of star formation, and their effect could last at least 10^8 yr with many shorter timescale bursts. Starburst nuclei and active galactic nuclei (AGNs) are not always associated with interacting galaxies (Balzano 1983; Keel & van Soest 1992), and the triggering mechanism of such activities is a long-standing problem (e.g., Taniguchi & Wada 1996; Taniguchi 1999). The recurrent bursts in our model could be a solution of this problem. Suppose a galaxy interacts with another galaxy or experiences a minor merger with one of its companions. Such phenomena can coherently trigger the initial starburst in the galaxy, and can then initiate recurrent bursts which could last several 10^8 yr, as long as the gas remains. During this prolonged burst period, the galaxy that initially triggers the bursts would be distant from the host galaxy or the trace of the minor merger would disappear. As a result, one could observe an isolated galaxy with starbursts or AGNs. The recurrent burst model is especially suitable for nuclear regions ($R < 100$ pc). The typical size of supernova remnants is not much smaller than the size of the region, and also the timescale of the supernovae ($\sim 10^6$ yr) is comparable to the rotational period of the region. Thus supernovae explosions can affect the whole nuclear region and form new stars almost simultaneously. In other words, the bursts in the nuclear region should occur periodically with small phase differences. Consequently, each recurrent burst in the nuclear regions should be sharp, and if one observes a galaxy with recurrent nuclear bursts in the active phase, the galaxy would be recognized as a "starburst" galaxy. On the contrary, many starburst regions in a galactic disk (>1 kpc) have different phases of the recurrent bursts; as a result the total star formation rate in the disk varies more chaotically.

In the present paper, we have not solved the vertical structure of the ISM. We believe that cold, dense gases will form filamentary structures also in three-dimensional space (cf. theoretical models: Nordlund & Padoan 1998; Korpi et al. 1999; and observations: Howk & Savage 2000). It is expected that the hot component behaves differently in three dimensions. The hot gas, which is above 10^6 K, cannot be confined to the disk plane (Rosen & Bregman 1995; Avillez 2000), and it would probably blow out from the disk plane. The scale height of the hot gas should be larger than the cold gas, therefore the radiative cooling would be less effective in the hot gas, in three dimensions. This may affect the interaction between the cold and hot components, and the feedback process on the ISM. However, since the gas mass of the hot components is only 0.3% of the total gas mass (see Fig. 8), the global dynamics would not be affected if we consider the blowout of the hot gas from the disk plane. In a subsequent paper, we will extend our method to three-dimensional modeling and investigate these problems.

7. CONCLUSIONS

We have developed a high-resolution two-dimensional hydrodynamic model which represents the multiphase interstellar medium and includes supernovae and stellar winds. The two-dimensional evolution of blast waves caused by supernovae in an inhomogeneous and nonstationary medium with global rotation is followed explicitly. The code is tested for various one-dimensional and two-dimensional problems. It is confirmed that the code is as good as the high-accuracy schemes, such as the PPM, but it is much simpler. A globally stable multiphase ISM, in which filamentary and clumpy structure and low-density cavities are a characteristic feature, is formed with a hot component of 10^6–10^8 K gas that is a direct consequence of the energy input from the feedback. The porous density structure and turbulent-like velocity structure are natural consequences of gravitational and thermal instabilities in the self-gravitating, rotationally supported gas disk. The phase diagram shows that turbulent pressure dominates the thermal pressure especially for higher density gas ($\Sigma_g > 10$ $M_\odot$ pc^{-2}).

We find that the total supernova rate in model star formation (model SF) fluctuates rapidly, by a factor of 10 (0.001–0.01 yr^{-1}) during 6×10^7 yr. The variation of the supernova rate looks chaotic but results from the triggering of star formation due to supernovae explosions in inhomogeneous, clumpy media. One triggering event, such as a galaxy-galaxy encounter, can cause a burst of star formation, and it could last at least 10^8 yr with rapid fluctuations of the supernova rate.

We also find that, in spite of its complexity in structure, the multiphase ISM exhibits a one-point probability density function (pdf) that is a perfect lognormal distribution for a wide range of the density, 10^2–10^6 $M_\odot$ pc^{-2}. As suggested by the phase diagram, this density range is a region where self-gravity of gas dominates the dynamics. The lognormal pdf is very robust for frequent SNe. We also find that the low-density regions, or cavities, have a different pdf described by a normal distribution, which may suggest different physics or statistical processes taking part in the formation of low-density regions. Alternatively, they might be understood by a single, but more general distribution function, such as Lévy distribution, which is the general distribution resulting from sums of independent variables. The energy spectrum of the velocity field of the star-forming model suggests that the medium is turbulent-like on a global scale, and shocks produced by frequent supernovae dominate the turbulent velocity field.

Large-scale effects of supernovae on the ISM have been discussed for many decades. Cox & Smith (1974), for example, suggested that the gaseous disk of our Galaxy is sufficient to generate and maintain a mesh of interconnected tunnels containing very low-density gas throughout the ISM. Although our global model of the ISM is a two-dimensional approximation, our results suggest that the interconnected tunnels of hot gas are not a direct consequence of the supernovae explosions, but rather they arise naturally from the nonlinear evolution of the self-gravitating, radiative interstellar gas. Supernovae are necessary for producing 10^6–10^7 K gas, but the structure of the multiphase ISM is naturally porous without SNe or stellar winds. H I cavities observed in many nearby spiral and dwarf galaxies should not always be direct evidence of the explosional phenomena. In the three-phase model of the ISM by McKee & Ostriker (1977), all phases of the medium are assumed to be kept in rough pressure equilibrium. Their approach succeeded significantly in constructing the steady state model of the ISM on a local scale. On the other hand, our global model suggests that the ISM is far from pressure

equilibrium and it is quite dynamic. This is a very important feature of the ISM particularly when one would like to investigate gas and star formation phenomena on a global scale, such as for galaxy formation, galaxy-galaxy interactions or mergers, galactic fountains, fueling for the nuclear starburst regions, and galactic shocks.

We are grateful to M. Spaans for providing us the cooling functions. We acknowledge many fruitful comments and suggestions by the anonymous referee, and also thank stimulating discussions with HOT TOPICS members at Johns Hopkins University. We also thank T. Yoshida, K. Tomisaka, and H. Fukuda for their contribution to our numerical codes. K. W. thanks Yamada Science Foundation for their support at STScI. Numerical computations were carried out on VPP300/16R and VX/4R at the Astronomical Data Analysis Center of the National Astronomical Observatory, Japan, and VPP700 at SUBARU Observatory, Hawaii. We would like to thank Ryusuke Ogasawara for his help at SUBARU observatory.

REFERENCES

Athanassoula, E. 1992, MNRAS, 259, 345
Avillez, M. A. D. 2000, MNRAS, in press (astro-ph/0001315)
Balzano, V. A. 1983, ApJ, 268, 602
Bania, T. M., & Lyon, J. G. 1980, ApJ, 239, 173
Bregman, J. D., Temi, P., & Rank, D. 2000, A&A, 355, 525
Colina, L., & Wada, K. 2000, ApJ, 529, 845
Cox, D. P., & Smith, B. W. 1974, ApJ, 189, L105
Dahlburg, R. B., Dahlburg, J. H., Gardner J. H., & Picone, J. M. 1990, Phys. Fluid A, 2, 1481
Deul, E. R., & den Hartog, R. H. 1990, A&A, 229, 362
Englmaier, P., & Gerhard, O. 1997, MNRAS, 287, 57
Fukuda, H., Wada, K., & Habe, A. 1998, MNRAS, 295, 463
Gazol-Patino, A., & Passot, T. 1999, ApJ, 518, 748
Gerritsen, J. P. E., & Icke, V. 1997, A&A, 325, 972
Harten, A. 1983, J. Comp. Phys., 49, 357
Heller, C. H., & Shlosman, I. 1994, ApJ, 424, 84
Hernquist, L., & Mihos, J. C. 1995, ApJ, 448, 41
Hockney, R. W., & Eastwood, J. W. 1981, Computer Simulation Using Particles (New York: McGraw Hill)
Howk, J. C., & Savage, B. D. 2000, AJ, 119, 644
Ikeuchi, S., Habe, A., & Tanaka, Y. D. 1984, MNRAS, 207, 909
Katz, N. 1992, ApJ, 391, 502
Keel, W. C., & van Soest, E. T. M. 1992, A&AS, 94, 553
Korpi, M. J., Brandenburg, A., Shukurov, A., & Tuominen, I. 1999, A&A, 350, 230
Kraichnan, R. H. 1967, Phys. Fluids, 10, 1417
Larson, R. B. 1981, MNRAS, 194, 809
Laughlin, G., Korchagin, V., & Adams, F. C. 1997, ApJ, 477, 410
———. 1998, ApJ, 504, 945
Leitherer, C., Robert, C., & Drissen, L. 1992, ApJ, 401, 596
Lindblad, P. O., & Lindblad, P. A. B. 1994, in ASP Conf. Ser. 66, Physics of the Gaseous and Stellar Disks of the Galaxy, ed. I. R. King (San Francisco: ASP), 29
Liou, M. 1996, J. Comp. Phys., 129, 364
Liou, M., & Steffen, C. 1993, J. Comp. Phys., 107, 23
McKee, C. F., & Ostriker, J. P. 1977, ApJ, 218, 148
Montroll, E. W., & Bendler, T. 1984, J. Stat. Phys., 34, 129
Montroll, E. W., & Shlesinger, M. F. 1983, J. Stat. Phys., 32, 209
Mori, M., Yoshii, Y., Tsujimoto, T., & Nomoto, K. I. 1997, ApJ, 478, L21
Navarro, J. F., & White, S. D. M. 1993, MNRAS, 265, 271
Nordlund, A., & Padoan, P. 1998, in Interstellar Turbulence, ed. J. Franco & A. Carraminana (Cambridge: Cambridge Univ. Press), 218
Norman, C. A., & Ferrara, A. 1996, ApJ, 467, 280
Norman, C. A., & Ikeuchi, S. 1989, ApJ, 345, 372
Padoan, P., Nordlund, A., & Jones, B. J. T. 1997, MNRAS, 288, 145
Passot, T., Pouquet, A., & Woodward, P. 1988, A&A, 197, 228
Passot, T., & Vázquez-Semadeni, E. 1998, Phys. Rev. E, 58, 4501
Passot, T., Vázquez-Semadeni, E., & Pouquet, A. 1995, ApJ, 455, 536
Roe, P. L. 1981, J. Comp. Phys., 43, 357
Rosen, A., & Bregman, J. N. 1995, ApJ, 440, 634
Rosen, A., Bregman, J. N., & Norman, M. L. 1993, ApJ, 413, 137
Ryu, D., Ostriker, J. P., Kang, H., & Cen, R. 1993, ApJ, 414, 1
Scalo, J., Vázquez-Semadeni, E., Chappell, D., & Passot, T. 1998, ApJ, 504, 835
Shore, S. N., & Ferrini, F. 1995, Fundam. Cosmic Phys., 16, 1
Sod, G. A. 1978, J. Comp. Phys., 27, 1
Sofue, Y., Tutui, Y., Honma, M., Tomita, A., Takamiya, T., Koda, J., & Takeda, Y. 1999, ApJ, 523, 136
Spaans, M., & Norman C. 1997, ApJ, 483, 87
Stone, J., & Norman, M. N. 1992, ApJS, 80, 753
Taniguchi, Y. 1999, ApJ, 524, 65
Taniguchi, Y., & Wada, K. 1996, ApJ, 469, 581
van Leer, B. 1977, J. Comp. Phys., 32, 101
Vázquez-Semadeni, E. 1994, ApJ, 423, 681
Vázquez-Semadeni, E., Gazol, A., & Scalo, J. 2000, ApJ, 540, 271 (VGS)
Vázquez-Semadeni, E., Pasot, T., & Pouquet, A. 1995, ApJ, 441, 702
———. 1996, ApJ, 473, 881
Wada, K. 1994, PASJ, 46, 165
Wada, K., & Habe, A. 1992, MNRAS, 258, 82
———. 1995, MNRAS, 277, 433
Wada, K., & Norman, C. A. 1999, ApJ, 516, L13 (Paper I)
Wada, K., Spaans, M., & Kim, S. 2000, ApJ, 540, 797
Walter, F., & Brinks, E. 1999, AJ, 118, 273
Woodward, P. R., & Colella, P. 1984, J. Comp. Phys., 54, 115 (WC84)
Yuan, C., & Cheng, Y. 1989, ApJ, 340, 216